Article

A Complete Picture of Cation Dynamics in Hybrid Perovskite Materials from Solid-State NMR Spectroscopy

Aditya Mishra, Michael A. Hope, Michael Grätzel, and Lyndon Emsley*

Read Online

ACCESS | 📊 Metrics & More | 📖 Article Recommendations | 🗎 Supporting Information

ABSTRACT: The organic cations in hybrid organic−inorganic perovskites rotate rapidly inside the cuboctahedral cavities formed by the inorganic lattice, influencing optoelectronic properties. Here, we provide a complete quantitative picture of cation dynamics for formamidinium-based perovskites and mixed-cation compositions, which are the most widely used and promising absorber layers for perovskite solar cells today. We use ^2H and ^{14}N quadrupolar solid-state NMR relaxometry under magic-angle spinning to determine the activation energy (E_a) and correlation time (τ_c) at room temperature for rotation about each principal axis of a series of organic cations. Specifically, we investigate methylammonium (MA$^+$), formamidinium (FA$^+$), and guanidinium (GUA$^+$) cations in current state-of-the-art single- and multi-cation perovskite compositions. We find that MA$^+$, FA$^+$, and GUA$^+$ all have at least one component of rotation that occurs on the picosecond timescale at room temperature, with MA$^+$ and GUA$^+$ also exhibiting faster and slower components, respectively. The cation dynamics depend on the symmetry of the inorganic lattice but are found to be insensitive to the degree of cation substitution. In particular, the FA$^+$ rotation is invariant across all compositions studied here, when sufficiently above the phase transition temperature. We further identify an unusual relaxation mechanism for the ^2H of MA$^+$ in mechanosynthesized FA$_x$MA$_{1-x}$PbI$_3$, which was found to result from physical diffusion to paramagnetic defects. This precise picture of cation dynamics will enable better understanding of the relationship between the organic cations and the optoelectronic properties of perovskites, guiding the design principles for more efficient perovskite solar cells in the future.
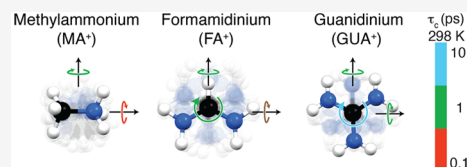
INTRODUCTION

Hybrid organic−inorganic perovskite materials have drawn significant attention owing to their pertinent optoelectronic properties for use in solar cells and LEDs.[1−3] Notably, the power conversion efficiencies (PCEs) of perovskite solar cells have already exceeded 25%,[4,5] rivaling conventional solar cell technologies at a lower cost.[6−8] These materials adopt the ABX$_3$ perovskite crystal structure, where A$^+$ is a monovalent cation—primarily methylammonium (MA$^+$, CH$_3$NH$_3^+$), formamidinium [FA$^+$, CH(NH$_2$)$_2^+$], guanidinium [GUA$^+$, C-(NH$_2$)$_3^+$], and/or Cs$^+$—that resides in the cuboctahedral cavity formed by corner-sharing lead halide octahedra (I$^-$, Br$^-$, and Cl$^-$) as illustrated schematically in Figure 1a.[9−15] The best-performing devices today use double-[4,16−21] or triple-cation compositions[22] with a mixture of different A-site cations, which increases the PCE[4,21,23,24] and stability[4,21,25,26] as compared to their single-cation analogues.

These materials exhibit a variety of complex atomic-level motions spanning a wide range of frequencies. This includes ion migration on long timescales (milliseconds to hours),[27,28] low energy polar (optical) vibrational modes of the metal-halide sublattice (up to ps),[29,30] and reorientation of the A-site cation within the cuboctahedral cavities of the inorganic lattice on a similar timescale (∼0.1−1 ps).[31−34] These multi-timescale structural dynamics affect key electronic properties such as exciton binding energies and charge-carrier mobilities.[14,35−41] The rotation of the A-site cation is particularly important

because it has also been shown to be linked with key phenomena such as efficient charge separation,[42] tolerance to intrinsic point defects,[43] and dynamic splitting of band extrema.[44]

Consequently, MA$^+$ cation dynamics have been widely explored through a range of techniques including quasi-elastic and inelastic neutron scattering,[45−49] dielectric spectroscopy,[27] millimeter-wave spectroscopy,[50] two-dimensional infrared spectroscopy,[51,52] and NMR spectroscopy.[31,53−56] The MA$^+$ cation dynamics have been further found to correlate strongly with the crystallographic perovskite phase evolution.[9] Among these techniques, NMR relaxometry and linewidth analysis have proved to be sensitive probes of both the nature and the rate of motion.[31,53−55,57] Notably, ^2H and ^{14}N quadrupolar relaxation measurements performed under static conditions have been used to determine the correlation times about each of the two unique principal axes of the MA$^+$ ion.[54]

In contrast, there has been much less focus on the dynamics of the FA$^+$ cation, despite it being the most widely used in
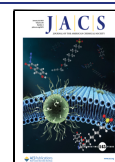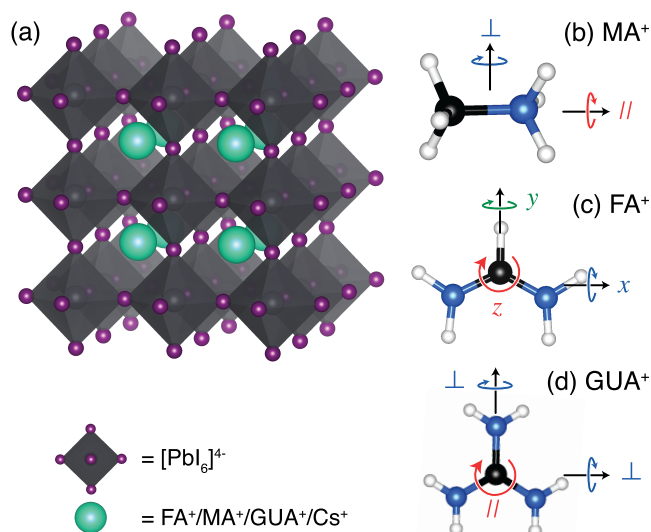
Figure 1. Perovskite crystal structure (a) and principal axes of rotation for the most commonly employed cations: (b) methylammonium (MA^+), (c) formamidinium (FA^+), and (d) guanidinium (GUA^+). H, C, and N atoms are represented by white, black, and blue balls, respectively.
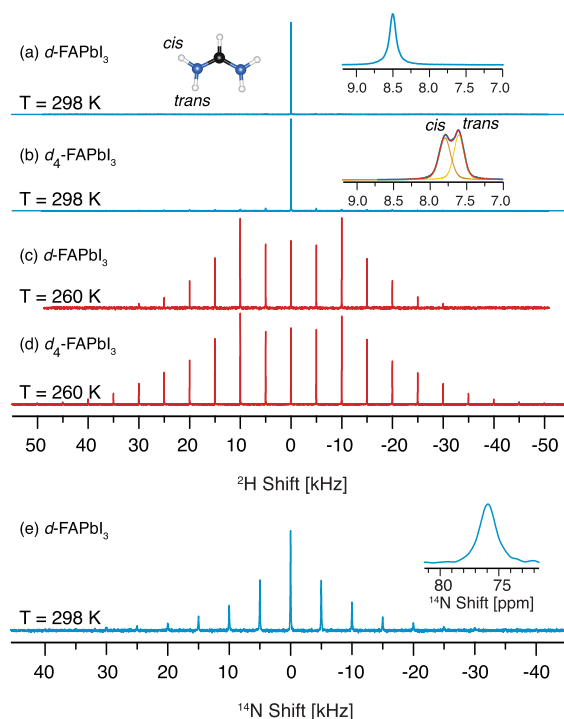

Figure 2. Single pulse solid-state ^2H MAS NMR spectra in the cubic phase of d-FAPbI$_3$ (a) and d_4-FAPbI$_3$ (b). The insets show a zoom of the isotropic resonances and the resolved peaks of the two ND$_2$ deuterons. ^2H MAS NMR spectra in the tetragonal phase (at 260 K) of d-FAPbI$_3$ (c) and d_4-FAPbI$_3$ (d). Hahn-echo detected ^{14}N MAS NMR spectra of d-FAPbI$_3$ (e). The inset shows a zoom of the central peak. All spectra were recorded at 5 kHz MAS; further experimental details are given in the Supporting Information.

optoelectronic applications.[4,58] Experimental studies using two-dimensional infrared spectroscopy[59] and low temperature neutron scattering[60] rely heavily on molecular dynamic simulations to aid interpretation. ^1H NMR relaxometry[32,61] and ^{14}N linewidth analysis[53] have been used to study FA^+ dynamics but with simple motional models that rely on a series of assumptions (Bloembergen−Purcell−Pound theory and model free analysis) and that yield only a single correlation time, while FA^+ motion is notably characterized by rotational rates about three distinct principal axes. Device-relevant multi-cation systems introduce additional experimental complexity. As a result, a complete picture of the dynamics in FAPbI$_3$ and mixed-cation perovskites is lacking.

Here, we use variable temperature, multi-nuclear ^2H and ^{14}N NMR relaxometry under magic angle spinning (MAS) to determine the rotational rates and activation energies for each distinct axis of FA^+, MA^+, and GUA^+ in a series of contemporary multi-cation perovskite compositions. MAS critically facilitates the study of lower symmetry cations and mixtures. We discover noticeably faster rotational dynamics for MA^+ in mixed FA^+/MA^+ compositions, whereas the FA^+ dynamics are essentially unaffected. In contrast, we find that the addition of Cs^+ into the FA^+ matrix does change the FA^+ motion at room temperature significantly, largely because of changes in the phase transition temperature. Further, extending the approach to a mixed GUA^+/MA^+ perovskite, we find that MA^+ rotation is again faster than in MAPbI$_3$ and that surprisingly GUA^+ also exhibits fast picosecond rotation, despite its bulky nature.

■ RESULTS

Symmetry and Phase Transitions of FAPbI$_3$. ^2H and ^{14}N are quadrupolar nuclei ($I = 1$) which yield NMR spectra that are very sensitive to the local symmetry.[62,63] To perform deuterium NMR measurements, deuterated FAPbI$_3$ was synthesized using d-FAI and d_4-FAI, with substitution of the CH and NH$_2$ hydrogens, respectively. Figure 2a,b shows the ^2H MAS spectra of d-FAPbI$_3$ and d_4-FAPbI$_3$ at room

temperature in the metastable, cubic black phase (α, $Pm\bar{3}m$). d-FAPbI$_3$ shows one peak at 8.5 ppm, as expected (inset, Figure 2a), whereas two isotropic shifts are observed for d_4-FAPbI$_3$, corresponding to the two inequivalent deuterons arising from restricted rotation of the C−N bond, as also seen by solution NMR.[64] These can be assigned in the fully deuterated d_5-FAPbI$_3$ sample using a ^2H−^2H EXSY experiment on the basis of their proximity to the CD deuteron (Figure S1).

Figure 2e shows the ^{14}N MAS spectrum at room temperature, where the quadrupolar coupling results in a spinning sideband manifold spanning a full-width at half-maximum of ∼20 kHz, which can be approximately fitted using a Czjzek model[65] (Figure S2), with an average C_Q of 27 kHz. This narrow width compared to the ^{14}N quadrupolar coupling constant (C_Q) for FA^+ of ∼2.7 MHz in the absence of any motion indicates that the cation undergoes almost, but not quite, isotropic reorientation, as expected at room temperature in the cubic cavity.[53]

The residual anisotropy is also visible as low-intensity spinning sidebands in the ^2H spectra (Figure S3), but the anisotropy is smaller for CD and the trans ND$_2$ deuteron than for the cis deuteron. This indicates that the anisotropy predominantly arises from preferred orientation of the x- and z-axes (using the axis scheme shown in Figure 1c); i.e., the S_{xx} and S_{zz} components of the order tensor are larger than the S_{yy} term, although the residual orientational order is very small, with $|S|$ on the order of 0.01. The similarity of the anisotropies for CD and the parallel ND$_2$ further corroborates the assignment of the ND$_2$ deuterons since they have similar

orientations within the molecule (noting that quadrupolar coupling is invariant to a 180° rotation).

Black FAPbI$_3$ is known to undergo a phase transition at ~285 K from the cubic phase to the tetragonal phase (β, P4/mbm).[66,67] This reduction in symmetry is clearly observed in the ^{2}H spectrum, which shows a significantly broader sideband manifold at 260 K (Figure 2c,d). This is associated with a distribution of quadrupolar coupling tensors corresponding to a distribution of motions with different orientational anisotropies. Due to the larger quadrupolar moment of ^{14}N, the ^{14}N spectrum becomes challenging to measure with conventional techniques in the β phase because the quadrupolar pattern becomes very broad.[61]

Motion on a similar timescale to the nuclear Larmor frequency (~10^8 Hz) induces longitudinal nuclear spin relaxation (T_1). ^{2}H and ^{14}N T_1 relaxation times are pertinent probes to investigate rotation as they depend upon the orientation of the electric field gradient (EFG) tensor with respect to the principal axes of rotation and can therefore differentiate the correlation times about different axes. Figure 3 shows the measured ^{2}H and ^{14}N T_1 constants for FAPbI$_3$, which are observed to decrease with decreasing temperature,

indicating that the cation rotation is in the so-called fast motion regime (faster than the Larmor frequency). As the characteristic timescale of the rotational motion slows down at lower temperatures, it becomes closer to the Larmor frequency and induces relaxation more effectively. Superimposed on this general trend, we observe discontinuities at 285 K corresponding to the $\alpha \leftrightarrow \beta$ first-order phase transition. In the following, we analyze the NMR relaxometry data in depth, exploiting the sensitivity of the T_1 relaxation to motion on this timescale to extract a detailed picture of the cation dynamics.

Rotational Dynamics in FAPbI$_3$. In order to extract motional rates from the relaxation data, a motional model is required. Here, we use the rotational diffusion model of Huntress[68] in which the orientation of the molecule is assumed to change randomly, resulting in overall rotational diffusion, analogously to the random translation that results in overall translational diffusion. This rotational diffusion is characterized by rotational diffusion constants (D_i) about the three principal axes of the molecule, which are in turn related to angular correlation times about the corresponding axes by $D = 1/(6\tau_c)$.[68] When the principal axes are not equivalent by symmetry, the rotational diffusion rates about these axes are different. Note that, even with different rotational rates about the three axes, this rotational diffusion model assumes an isotropic orientational distribution.[68] Although as discussed above the orientation of FA$^+$ in FAPbI$_3$ is not quite isotropic, the very small residual orientational order would be a negligibly minor correction to the model. We note that the rotational diffusion model has previously been applied to MAPbI$_3$ in the tetragonal phase, which has a much larger residual orientational order.[54]

Quadrupolar T_1 relaxation depends on the rotational diffusion rate about each axis, the size of the quadrupolar coupling, and the orientation of the quadrupolar coupling tensor with respect to the principal axes of the rotational diffusion tensor. Expressions for quadrupolar relaxation under rotational diffusion have been derived by Huntress;[68] in the case of the planar FA$^+$ cation, the ^{2}H relaxation is given by

(a)

^{2}H T_1 [s]

CD
trans
cis

Cubic ⟷ Tetragonal

(b)

^{14}N T_1 [s]

Cubic ⟷ Tetragonal
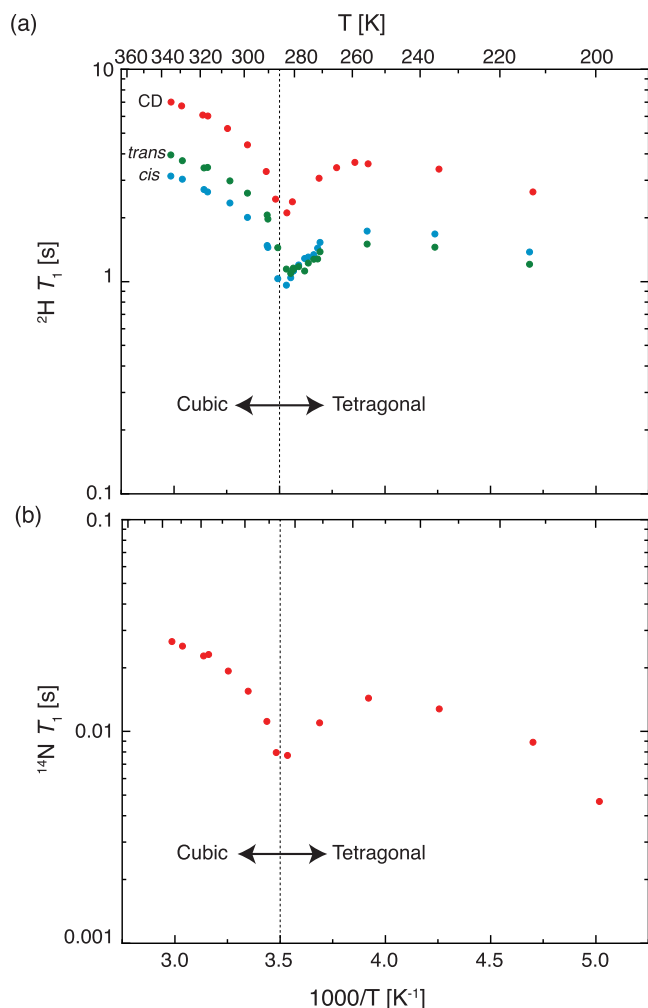
1000/T [K^{-1}]

Figure 3. Measured ^{2}H and ^{14}N longitudinal relaxation time constants (T_1) of black FAPbI$_3$ as a function of temperature. The discontinuities in the T_1 behavior are indicative of the crystallographic phase transition of the material. Experimental details are given in the Supporting Information.

$$\frac{1}{T_1(^2\text{H})} = \frac{1}{32}\frac{(2\pi C_Q)^2}{D_r}\left\{[4D_x + (\eta - 1)^2 D_y \right.$$
$$+ (\eta + 1)^2 D_z]\cos^2\phi$$
$$+ [4D_y + (\eta - 1)^2 D_x + (\eta + 1)^2 D_z]\sin^2\phi$$
$$\left. - \frac{(\eta - 3)^2}{3}\frac{(D_x - D_y)^2}{D_z + D_s}\cos^2\phi\,\sin^2\phi\right\}$$

$$D_r = D_x D_y + D_x D_z + D_y D_z,$$

$$D_s = \frac{1}{3}(D_x + D_y + D_z)$$

(1)

where C_Q is the quadrupolar coupling constant in units of Hz, η is the quadrupolar asymmetry, ϕ is the angle between the EFG principal axis V_{zz}^{2H} (along the deuterium bond), and the x-axis of the diffusion tensor. For ^{14}N, where the principal component of the EFG tensor is perpendicular to the plane, T_1 is given by

$$\frac{1}{T_1(^{14}\mathrm{N})} = \frac{1}{32}\frac{(2\pi C_\mathrm{Q})^2}{D_\mathrm{r}}\Bigg\{[4D_z + (\eta + 1)^2 D_y$$
$$+ (\eta - 1)^2 D_x]$$
$$\cos^2\phi'$$
$$+ [4D_z + (\eta + 1)^2 D_x + (\eta - 1)^2 D_y]\sin^2\phi'$$
$$- \frac{4\eta^2}{3}\frac{(D_x - D_y)^2}{D_z + D_s}\cos^2\phi'$$
$$\sin^2\phi'\Bigg\}$$

$$(2)$$

where ϕ' is the angle between $V_{xx}^{14\mathrm{N}}$ and the x-axis of the diffusion tensor.

The quadrupolar parameters used here for the ^{2}H and ^{14}N nuclei in FA$^+$ are given in Table 1 (see also Figure S18). It is

Table 1. Nuclear Quadrupolar Tensor Parameters for FA$^+$

Nucleus	C_Q (MHz)	η	ϕ (deg)
^{14}N	2.7 ± 0.2	0.26	55.5
^{2}H-CD	0.165 ± 0.005	0.16	90
^{2}H ND$_2$-trans	0.207 ± 0.005	0.17	−84.2
^{2}H ND$_2$-cis	0.207 ± 0.005	0.17	32.8

the quadrupolar coupling constant in the absence of motion that dictates the quadrupolar relaxation, and to measure this experimentally, all motion must be frozen out. However, in FAPbI$_3$, even at ∼100 K, the motion is not completely arrested (see Figure S4). To counter this, we measured the ^{2}H quadrupolar couplings in d-FAI and d_4-FAI at 100 K (Figures S5 and S6) and use those values as proxies. The ^{14}N quadrupolar coupling is challenging to measure due to the large width of the quadrupolar pattern. Therefore, we have used the value calculated from density functional theory by Kubicki et al. of 2.7 MHz.[53] We note that Mozur et al. calculated a C_Q of 2.8 MHz in FAPbBr$_3$,[61] and we have calculated C_Q = 2.4 MHz in FACl; therefore, we estimate an uncertainty of ∼0.2 MHz.

To extract the rotational rates about the three axes, the T_1 constants of all three deuterons and ^{14}N must be combined; therefore, we measured these for perdeuterated d_5-FAPbI$_3$ (Figure 4a). As the cubic α-FAPbI$_3$ phase is the most relevant to photovoltaic applications, we focus on the temperature range 290−340 K. At each temperature, the four T_1 constants were combined to give D_x, D_y, and D_z using the above equations (Figure 4b). The resulting T_1 constants (dashed lines in Figure 4a) match the experimental data extremely well, lending confidence in the model. The determined rotational diffusion constants show an Arrhenius dependence above 305 K, below which deviation is observed due to the nearby first-order phase transition[32,66,67] (cf. Figure 3). Arrhenius analysis gives the activation energies (E_a) about each axis independently (Table 2). Using the relation $D = 1/(6\tau_c)$, the correlation time about each axis was calculated at 298 K (Table 2) from the data shown in Figure 4b; note that due to non-Arrhenius behavior near the phase transition, the correlation time was interpolated directly from the adjacent data, not taken from the Arrhenius analysis. The motion about all three axes is on the
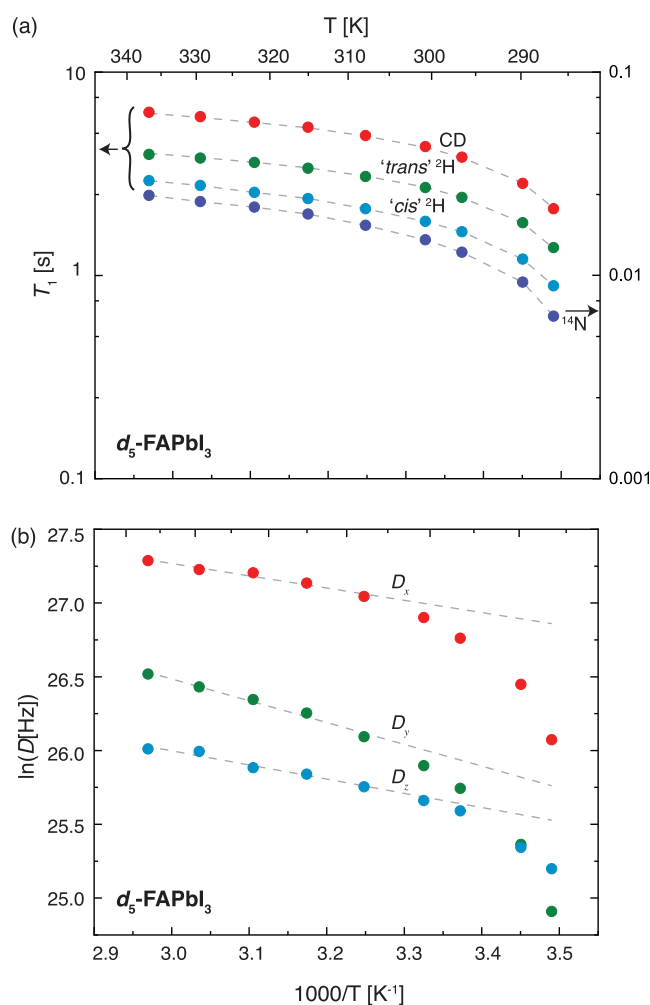

Figure 4. d_5-FAPbI$_3$ NMR relaxometry and rotational diffusion rates. (a) Three ^{2}H and one ^{14}N T_1 constants measured as a function of temperature in the cubic phase. Dashed lines indicate the fit to the rotational diffusion model. (b) Arrhenius plot of the rotational diffusion constants derived from (a). Dashed lines indicate fits to the Arrhenius behavior. Only the five highest temperature points were considered in the Arrhenius fits as the phase transition at ∼285 K causes deviation from Arrhenius behavior.

Table 2. Activation Energy (E_a) and Correlation Time at 298 K (τ_c) Determined Here for Rotation about Each Axis of FA$^+$ in FAPbI$_3$ Using the Axis System Shown in Figure 1

Axis	E_a (meV)	τ_c (ps), 298 K
x	62 ± 17	0.38 ± 0.08
y	130 ± 16	1.05 ± 0.24
z	99 ± 26	1.3 ± 0.5

picosecond timescale, with the fastest rotation about the x-axis, as predicted by Fabini et al. using molecular dynamics simulations[61] and in line with the relative moments of inertia $I_x < I_y < I_z$.[69]

FA$^+$ Dynamics in Cs$^+$-Alloyed Perovskite Compositions. Alloying FAPbI$_3$ with a small amount of Cs$^+$ is the best strategy to date to suppress the detrimental processes of ion migration and light-induced phase segregation in mixed-halide perovskites, which limit device performance and lifetimes.[25,58,70−74] In order to assess the changes in the FA$^+$ dynamics on Cs$^+$ substitution, d_5-FAPbI$_3$ was substituted with

5% Cs^+ as confirmed by ^{133}Cs MAS NMR[75] (Figure S7). Compared to pristine $FAPbI_3$, we note that the phase transition temperature was raised to 300 K, consistent with prior work.[66] The ^2H T_1 is shorter for the Cs^+/FA^+ composition around room temperature, indicating that the motion is slower due to the vicinity of the phase transition (Figures 4 and S27, Table S2). However, at higher temperatures, the T_1 time constants for $FAPbI_3$ and $Cs_{0.05}FA_{0.95}PbI_3$ are the same within error, suggesting that there is no significant change in the energy landscape for the FA^+ rotation (Figure S26).

Further alloying with MA^+ to yield a triple-cation composition[22] does not significantly change the experimental $FA^+ T_1$ values (Figure 5). We conclude that FA^+ dynamics are similar in the single-, double-, and triple-cation compositions.

FA^+ Dynamics in FA^+/MA^+ Perovskites. To explore the effect of MA^+ doping on the cation dynamics directly, we synthesized deuterated $FA_xMA_{1-x}PbI_3$ perovskite compositions. First, we determine the FA^+ dynamics. As shown in Figure 6a, all four deuterium signals are resolvable, allowing all
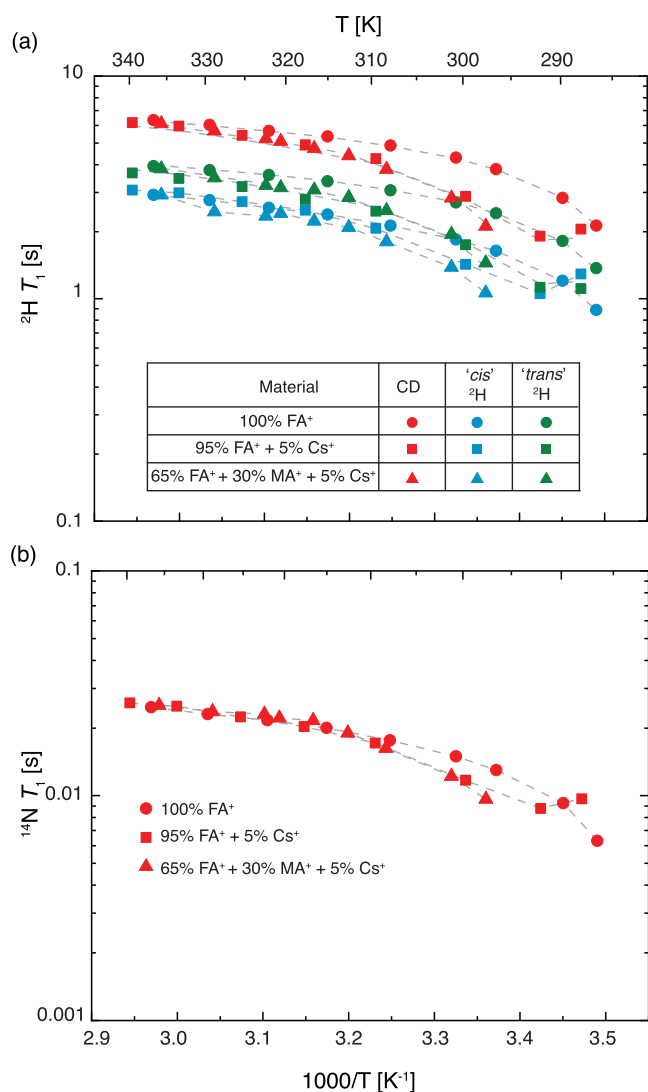
Figure 5. FA^+ dynamics in Cs-alloyed perovskite compositions. Experimentally measured (a) ^2H and (b) ^{14}N T_1 as a function of inverse temperature. Dashed lines represent fitted T_1 values using the rotational diffusion model.
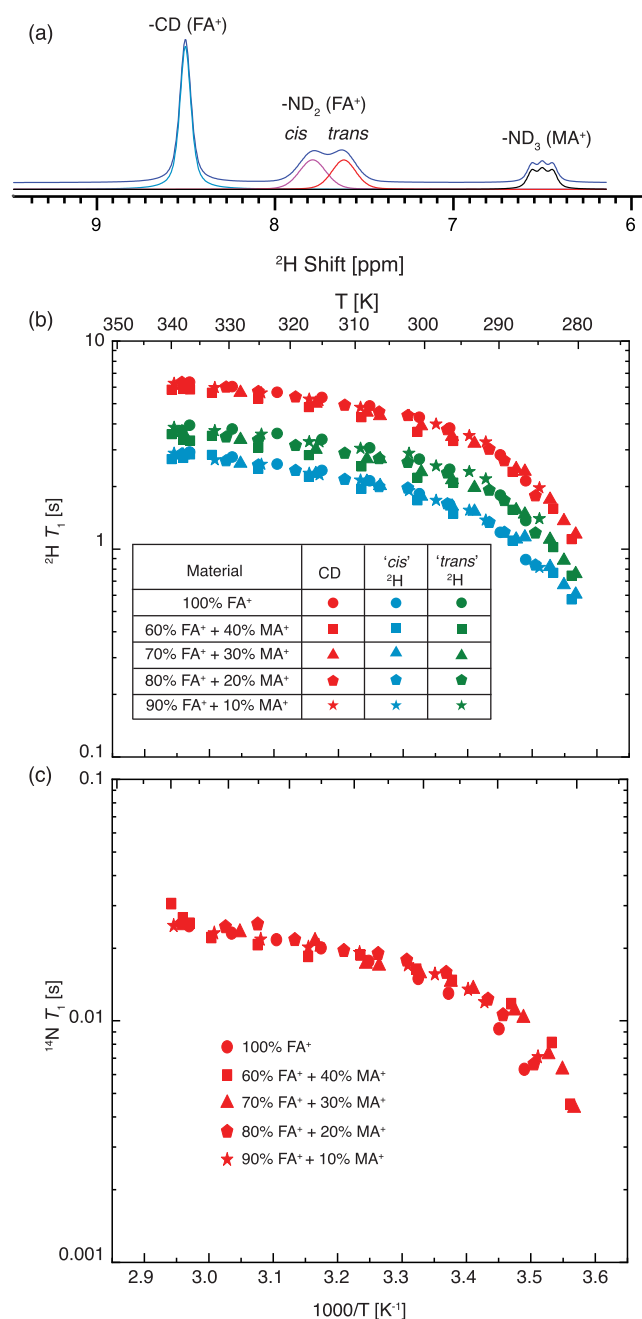
Figure 6. FA^+ dynamics in $FA_xMA_{1-x}PbI_3$ perovskite compositions. (a) Single pulse solid-state ^2H MAS NMR spectra of the cubic phase of $FA_{0.70}MA_{0.30}PbI_3$. The MA^+ peak shows J-coupling of $^1J(^2H-^{14}N)$ = 8.25 Hz. The deconvolution of all four sites is shown below the spectrum. Experimentally measured (b) ^2H and (c) ^{14}N T_1 as a function of inverse temperature and as a function of x in $FA_xMA_{1-x}PbI_3$.

the necessary ^2H and ^{14}N T_1 constants to be measured. The ^{14}N sideband manifold of FA^+ is broader than in pure $FAPbI_3$ (Figure S8) because MA^+ substitution breaks the local cubic symmetry. The ^{14}N sideband manifold of MA^+ is narrower than that of FA^+ due to the smaller C_Q of the former, but still broader than the isotropic signal observed in the cubic phase of pure $MAPbI_3$ due to the presence of FA^+. As shown in Figure 6b,c, the ^2H and ^{14}N relaxation times for FA^+ are largely unchanged as the composition is changed to include up to 40% MA^+, indicating that the FA^+ cation dynamics in the cubic

phase are essentially unaltered by MA$^+$ substitution (see Figures S24 and S25). Unlike for Cs$^+$ doping, there is little change in the $\alpha \leftrightarrow \beta$ phase transition temperature for FAPbI$_3$ upon MA$^+$ substitution.[60,76]

MA$^+$ Dynamics in FA/MA Perovskites. Having analyzed the FA$^+$ dynamics in mixed compositions, we now turn to MA$^+$. Surprisingly, mechanosynthesized FA$_{0.7}$MA$_{0.3}$PbI$_3$ exhibits a maximum in the ^{2}H T_1 at 310 K (Figure 7). As discussed
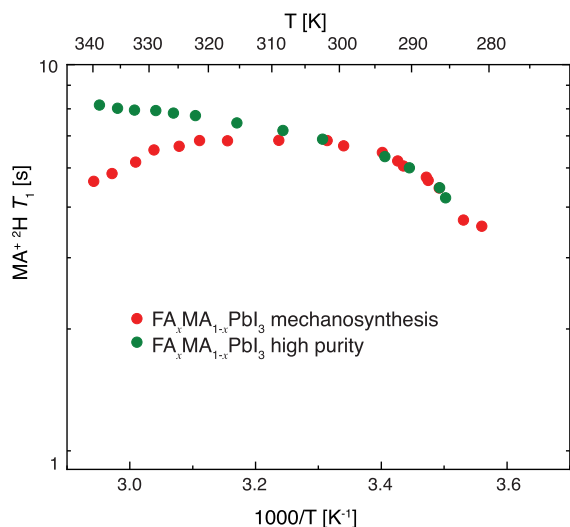

Figure 7. ^{2}H relaxation times (T_1) of MA$^+$ in FA$_x$MA$_{1-x}$PbI$_3$ prepared using either mechanosynthesis or a solution-based high-purity protocol as described in the text.

above, the cations are rotating faster than the Larmor frequency ($\omega_0 \tau_c \ll 1$), and this fast-motion limit is characterized by a T_1 that increases with increasing temperature. However, above 310 K, T_1 decreases. This intriguing effect is consistently observed across different batches and different FA$^+$/MA$^+$ compositions (Figures S9–S12).

T_1 maxima have previously been observed for ^{1}H, ^{13}C, and ^{15}N in pure MAPbI$_3$ and were ascribed to the contribution of spin–rotation relaxation, which becomes more efficient at high temperatures.[57] However, since the spin–rotational relaxation rate is proportional to the square of the nuclear magnetic moment, protons on the MA$^+$ which are subject to the same rotation should relax $(\gamma_{1H}/\gamma_{2H})^2 = 42$ times faster than deuterium spins.[77] Contrary to this, we observed that MA^{+1}H relaxation is slower than ^{2}H relaxation, even after accounting for the equilibration of T_1 by fast spin-diffusion between MA$^+$ and FA$^+$ moieties (Figures S13 and S14). This clearly rules out an appreciable contribution of spin–rotation to the ^{2}H T_1.

Alternatively, the T_1 maximum could be caused by a separate slow-motion process that becomes dominant above 310 K, since in the slow-motion regime, T_1 decreases with increasing temperature. This can be readily checked by testing the expected $T_1 \propto \omega_0^2$ field dependence of a slow-motion process.[78] However, the measured ^{2}H T_1 constants at 21.1 and 11.7 T are essentially identical (Figure S15). Therefore, a slow-motion contribution to the ^{2}H T_1 can also be ruled out.

To propose a mechanism for the ^{2}H T_1 maximum, we consider that the measured ^{1}H relaxation times in solids are often limited by ^{1}H–^{1}H spin diffusion to relaxation sinks such as paramagnetic impurities, which cause rapid relaxation of

nearby protons.[79,80] We find this to be the case for mechanosynthesized MAPbI$_3$, for which the ^{1}H T_1 can be increased by deuteration to suppress ^{1}H–^{1}H spin diffusion (Figure S14). Furthermore, above the T_1 maximum, the ^{2}H T_1 varies somewhat between samples and over time (Figures S10–S12), suggesting the role of defects or impurities. Although ^{2}H–^{2}H spin diffusion is very slow (owing to the lower gyromagnetic ratio and lower concentration), physical diffusion of MA$^+$ and/or H$^+$ is well known in the literature and could potentially cause a similar effect. At higher temperatures, physical diffusion becomes faster, so that a deuteron would encounter a paramagnetic defect more quickly, on average, resulting in a shorter relaxation time. We note that this proposed mechanism would be field independent, because although the diffusion is slower than the Larmor frequency, it is not the spectral density of motion driving the relaxation, but rather it is the interaction with paramagnetic defects. To test this hypothesis, we prepared a high-purity sample by solution processing (see the Experimental Section in the Supporting Information) with a lower concentration of paramagnetic relaxation sinks as evidenced by the longer ^{1}H T_1 (Figure S17). At lower temperatures, the ^{2}H T_1 constants of the two samples are the same (Figure 7), but the high-purity sample does not exhibit a T_1 maximum and the T_1 increases monotonically with temperature. This corroborates the proposed mechanism of physical diffusion to paramagnetic defects for the ^{2}H T_1 maximum in the mechanosynthesized sample. See Note S1 for further discussion of this effect.

Having removed the unusual ^{2}H T_1 maximum, the ^{2}H T_1 of the high purity mixed FA$^+$/MA$^+$ sample is now induced purely by quadrupolar relaxation and can be used as a straightforward reporter of dynamics. We measured the ^{2}H and ^{14}N T_1 as a function of temperature and compared them with pristine MAPbI$_3$, as shown in Figure 8. Note that in MA$^+$, the ^{14}N T_1 only depends upon the motion of the C–N bond (caused by the perpendicular rotation illustrated in Figure 1b) as the EFG tensor is axially symmetric along the C–N bond and invariant to the C_3-rotation (Figure S18), whereas the ^{2}H T_1 is induced by both parallel and perpendicular rotations.[54] Unlike the FA$^+$ motion, which was unaffected by MA$^+$ substitution, we observed that both the ^{2}H T_1 and ^{14}N T_1 of MA$^+$ in FA$_{0.78}$MA$_{0.22}$PbI$_3$ are higher than in pristine MAPbI$_3$. In order to extract the rates about both axes, we applied the rotational diffusion model, using the equations of Bernard et al.[54] (see Table S1 and eqs S1, S2). As shown in Figure 8, the rotational diffusional model reproduces very well the experimental data. The activation energies from Arrhenius analysis and the correlation times at 298 K are shown in Table 3 for each axis. The parallel (C_3) rotation rate is unchanged for MA$^+$ in the mixed sample and, as previously found by Bernard et al. for pure MAPbI$_3$, appears to be an essentially unactivated process. This shows that in both materials, the parallel rotation of MA$^+$ is unhindered. Since the perpendicular rotation can be determined from the ^{14}N T_1 alone (and the ^{14}N relaxation is too fast to be affected by paramagnetic defects as observed above for ^{2}H), this was measured for all the mechanosynthesized compositions (Table 3). We find that while the activation energy for the perpendicular rotation of MA$^+$ is similar for pure MAPbI$_3$ and MA$_x$FA$_{1-x}$PbI$_3$, the motion is faster by a factor of $\sim$2 when MA$^+$ is substituted into FAPbI$_3$, with τ_c (298 K) changing from 1.95 to $\sim$1.0 ps. Furthermore, the correlation time is found to be independent of the MA$^+$ concentration up to 40% MA$^+$.
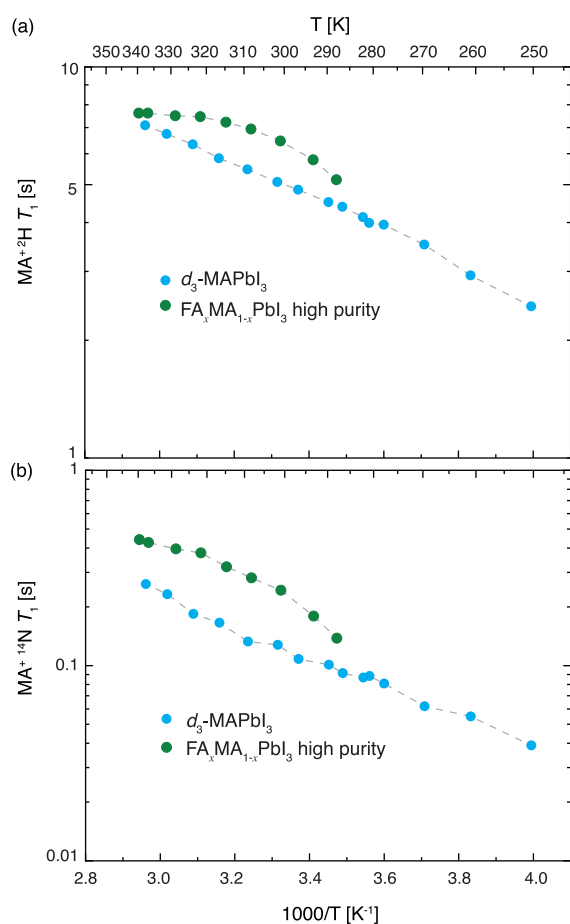
Figure 8. Experimentally measured (a) ^2H and (b) ^{14}N T_1 constants as a function of inverse temperature in MAPbI$_3$ and high-purity FA$_{0.78}$MA$_{0.22}$PbI$_3$. Dashed lines indicate fits to the rotational diffusion model.

Table 3. Dynamic Parameters of MA$^+$ in MA$_x$FA$_{1-x}$PbI$_3$

Material	E_a (meV)	τ_c (ps), 298 K
MAPbI$_3$	$\perp$: 156 ± 7	$\perp$: 1.95 ± 0.04
	$\parallel$: ~0	$\parallel$: 0.15 ± 0.04
FA$_{0.78}$MA$_{0.22}$PbI$_3$(high-purity)	$\perp$: 141 ± 10	$\perp$: 1.06 ± 0.03
	$\parallel$: ~0	$\parallel$: 0.16 ± 0.03
FA$_{0.90}$MA$_{0.10}$PbI$_3$ (mechanosynthesis)		$\perp$: 0.96 ± 0.02
FA$_{0.80}$MA$_{0.20}$PbI$_3$ (mechanosynthesis)		$\perp$: 0.98 ± 0.01
FA$_{0.70}$MA$_{0.30}$PbI$_3$ (mechanosynthesis)		$\perp$: 0.99 ± 0.02
FA$_{0.60}$MA$_{0.40}$PbI$_3$ (mechanosynthesis)		$\perp$: 1.10 ± 0.02

MA$^+$ and GUA$^+$ Dynamics in MA$_x$GUA$_{1-x}$PbI$_3$. Incorporation of the GUA$^+$ ion in the MAPbI$_3$ perovskite has been shown to provide improved performance, specifically long charge-carrier lifetimes,[81] high open-circuit voltage,[81,82] efficient charge transfer,[83] and increased stability.[11] This may be related to the absence of dipole moment in GUA$^+$, which has been suggested computationally to minimize the hysteresis in perovskite solar cells caused by cation motion.[84]

Here, we investigated the GUA$^+$ and MA$^+$ dynamics for the MA$_{0.75}$GUA$_{0.25}$PbI$_3$ composition. Although the room temperature phase of MAPbI$_3$ is tetragonal, substitution with the GUA$^+$ ion has been shown to decrease the phase transition temperature from 326 to 280 K for 20% GUA$^+$. However, despite the global cubic symmetry at room temperature, substitution with GUA$^+$ breaks the local symmetry, resulting in

orientational anisotropy for both MA$^+$ and GUA$^+$. This anisotropy can clearly be seen from the large residual quadrupolar coupling in the ^2H and ^{14}N spectra (Figures S19 and S20). Nevertheless, the signals from GUA$^+$ and MA$^+$ can be distinguished in both the ^2H and ^{14}N NMR spectra (Figure S21). Due to the considerable residual ^{14}N quadrupolar coupling for GUA$^+$, it is challenging to saturate the spectrum in order to measure the ^{14}N T_1. Therefore, we used a long phase-modulated pulse to saturate the broad ^{14}N pattern[85] (details in the Supporting Information).

Figure 9a shows the experimentally measured ^2H and ^{14}N T_1 relaxation times of MA$^+$ as a function of temperature in the
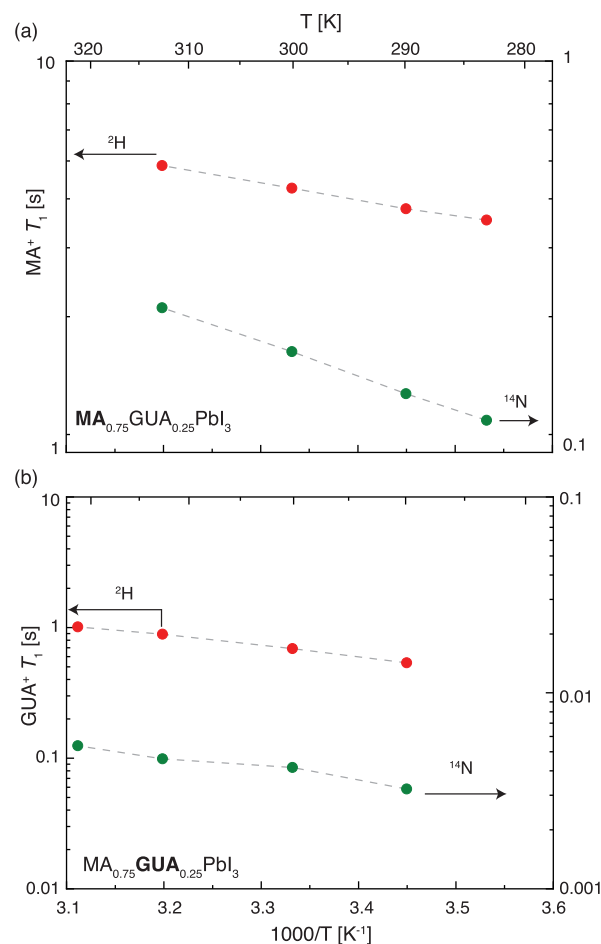

Figure 9. ^2H and ^{14}N T_1 constants of (a) MA$^+$ and (b) GUA$^+$ as a function of inverse temperature in MA$_{0.75}$GUA$_{0.25}$PbI$_3$ at 20 kHz MAS. Dashed lines indicate fits to the rotational diffusion model.

room temperature phase. The T_1 behavior is consistent with the expected MA$^+$ motion in the fast motion limit. Applying the rotational diffusion model to this relaxation data, we found that, similar to mixed MA$^+$/FA$^+$ compositions, the MA$^+$ parallel motion remains unactivated and at a similar rate upon GUA$^+$ substitution as in the pure MA$^+$ formulation (Table 4). The perpendicular motion also has a similar activation energy barrier as in MAPbI$_3$ (Table 4); however, again we found that the correlation time for the perpendicular motion at 298 K becomes faster with GUA$^+$ doping, as observed for MA$^+$ in the MA$^+$/FA$^+$ compositions.

Now we consider the motion of the guanidinium cation. GUA$^+$ is characterized by two distinct principal axes (Figure

Table 4. Dynamic Parameters of MA$^+$ and GUA$^+$ in MA$_x$GUA$_{1-x}$PbI$_3$

Material	E_a (meV)	τ_c (ps), 298 K
MAPbI$_3$	⊥: 156 ± 7	⊥: 1.95 ± 0.04
	∥: ~0	∥: 0.15 ± 0.04
MA$_{0.75}$GUA$_{0.25}$PbI$_3$	⊥: 168 ± 11	⊥: 1.32 ± 0.03
	∥: ~0	∥: 0.25 ± 0.03
MA$_{0.75}$**GUA**$_{0.25}$PbI$_3$	⊥: 121 ± 30	⊥: 1.27 ± 0.08
	∥: —	∥: 14 ± 8

1d) owing to the C_3 symmetry. The ^{14}N and ^{2}H quadrupolar relaxation constants are determined by the rotation about these axes according to

$$\frac{1}{T_1^Q(^2\text{H})} = \frac{1}{32}\frac{(2\pi C_Q)^2}{D_r}[4D_\perp + (\eta - 1)^2 D_\perp$$
$$+ (\eta + 1)^2 D_\parallel] \qquad (3)$$

$$\frac{1}{T_1^Q(^{14}\text{N})} = \frac{1}{16}\frac{(2\pi C_Q)^2}{D_r}[2D_\parallel + (\eta^2 + 1)D_\perp]$$

$$D_r = D_\perp^2 + 2D_\perp D_\parallel \qquad (4)$$

where C_Q is the quadrupolar coupling constant in units of Hz, and η is the quadrupolar asymmetry. The GUA$^+$ quadrupolar parameters used here are shown in Table 5.

Table 5. Nuclear Quadrupolar Tensor Parameters for GUA$^+$

Nucleus	C_Q (MHz)	η
^{14}N[a]	3.5 ± 0.3	0.4
^{2}H[b]	0.20 ± 0.01	0.14

[a]Averaged from nuclear quadrupole resonance experiments on different guanidinium salts.[86] [b]Experimental values for guanidinium chloride.[87]

Figure 9b shows the ^{2}H and ^{14}N T_1 relaxation data along with fits to the rotational diffusion model of eqs 3 and 4. The resulting activation energies and correlation times at 298 K are shown in Table 4. We find that the perpendicular rotation is on the picosecond timescale, which is similar to the other cations considered above. The parallel motion is slower than the perpendicular motion, which is consistent with the larger moment of inertia. However, we note that the parallel motion determined by this model is extremely sensitive to the input parameters, in particular the experimentally measured ^{14}N T_1 and the value of the static ^{14}N C_Q, which are both associated with large uncertainties. As discussed above, the ^{14}N spectrum of GUA$^+$ has a very broad pattern, resulting in a low signal-to-noise ratio and difficulties in accurately measuring T_1. Moreover, the ^{14}N static C_Q parameters are averaged from experimental nuclear quadrupole resonance studies for different guanidinium compounds, which could change to some degree in this sample. Consequently, there is a large uncertainty in the parallel correlation time at room temperature, and it was not possible to determine an activation energy for the parallel motion.

DISCUSSION

In summary, we have experimentally determined the rotational rates about each axis in FA$^+$, MA$^+$, and GUA$^+$ for different perovskite compositions (Figure 10).
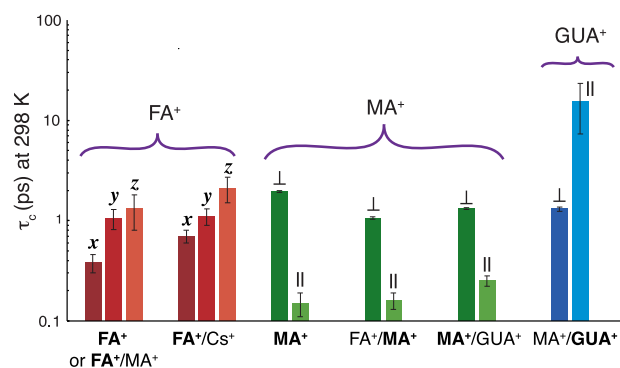

Figure 10. Comparison of experimentally measured rotational correlation times at room temperature for MA$^+$, FA$^+$, and GUA$^+$ cations in the various iodoplumbate perovskite compositions studied in this work. The corresponding activation energies are shown in Figure S22.

Despite these observed differences in rotation about the internal axes, there is at least one component of rotation for all three cations on the picosecond timescale. This similar timescale of the motion is surprising given the differences in dipole moment (GUA$^+$: 0 D, FA$^+$: 0.2 D, and MA$^+$: 2.3 D),[42] effective ionic radius (GUA$^+$: 278 pm, FA$^+$: 253 pm, and MA$^+$: 217 pm),[88,89] and lattice parameters (Table S3). The fastest motion we observe is the C_3 parallel rotation of MA$^+$ ($\tau_c = 0.16 \pm 0.03$ ps), which is consistent with it having the smallest moment of inertia and the apparent absence of any energy barrier to rotation. The slowest motion is the C_3 parallel rotation of GUA$^+$ ($\tau_c = 15 \pm 8$ ps), which is consistent with it having the largest moment of inertia, although we note the large error associated with this value.

Fabini et al.[32] also noted the similarity of the rotational rates of MA$^+$ and FA$^+$, based on a single correlation time determined from ^{1}H NMR relaxometry. However, their values (8 and 7 ps for FA$^+$ and MA$^+$ at room temperature, respectively) were significantly larger than those determined using ^{2}H and ^{14}N relaxometry here (and by Bernard et al.[54] for MAPbI$_3$). We propose that while this reflects the same physical phenomenon, i.e., the similarity of the rotational dynamics, the numerical discrepancy may arise from considering a single correlation time or the challenges in applying BPP theory away from the T_1 minimum.[90]

Here, we note that we have analyzed our data using an anisotropic rotational diffusion model, which corresponds to an isotropic continuum of possible cation orientations but with different rotational rates about each axis. This is in line with MD simulations of MA$^+$ rotation in MAPbI$_3$.[91] In contrast, Chen et al. reported that a $C_3 \otimes C_4$ jump model, combining threefold jumps about the parallel axis and fourfold jumps about the perpendicular axis (Figure 1b), was a better fit to their neutron scattering data than an isotropic rotational model[47] (a $C_3 \otimes O$ model with octahedral perpendicular jumps also gave indistinguishable results in the cubic phase). Based on the completely averaged ^{2}H and ^{14}N quadrupolar tensors in the experimental spectra of MAPbI$_3$ in the cubic phase, the perpendicular motion must have cubic or higher symmetry, but

it is not possible to distinguish between octahedral jumps or rotational diffusion on this basis. To compare, we modeled the ^{2}H and ^{14}N T_1 relaxation of MA$^+$ in MAPbI$_3$ at 330 K using a jump model, as implemented in the Express software package.[92] However, this yielded an unphysical correlation time for the C_3 jumps of 0.008 ps (see Note S2). Therefore, we conclude that the rotational diffusion model is a better fit to the experimental data. Nevertheless, at the current level of our analysis, we cannot discount a preferred orientation of the cations within the cage during rotational diffusion, if this preferred orientation has cubic symmetry.

To utilize ^{2}H NMR relaxometry, (partially) deuterated cations were used in this work, and it is important to note that the greater moment of inertia will result in slower cation rotation.[46] This effect is the greatest for the C_3 (parallel) rotation of MA$^+$, since the moment of inertia is entirely determined by the hydrogens, whereas the effect is significantly smaller for the perpendicular MA$^+$ rotation and for the other cations. The increase in moment of inertia is also mitigated here by the use of relatively low deuteration, typically ∼20%. Changes in the phase transition temperatures[93] and coupling to the inorganic lattice[46,94] have been observed in other hybrid perovskites on deuteration; however, since here we focus on the dynamics in the cubic phase near room temperature, this is not expected to have a significant effect. In particular, we note that there is no observable difference in the ^{2}H T_1 constants for two different levels of deuteration in MAPbI$_3$, to within the accuracy of the measurements (Figure S16), suggesting that any isotope effect is small. We believe that the trends we identify here are directly relevant to the fully protonated analogues used in photovoltaic devices.

Kubicki et al. previously reported that the MA$^+$ and FA$^+$ dynamics in FA$_{0.67}$MA$_{0.33}$PbI$_3$ are the same as in MAPbI$_3$ and FAPbI$_3$, respectively.[53] However, the correlation times deduced for MA$^+$ were 2−3 orders of magnitude longer than those determined here and by Bernard et al.[54] We ascribe this discrepancy to difficulties in relating measured ^{14}N linewidths to the motionally induced T_2 relaxation in their model-free analysis.

Considering the different compositions together, consistently it appears that cation substitution does not directly affect the cation dynamics. Both the FA$^+$ and MA$^+$ dynamics are unchanged throughout the mixed FA$_x$MA$_{1-x}$PbI$_3$ compositions studied, up to $x = 40\%$. Similarly, the FA$^+$ dynamics in FA$^+$/Cs$^+$ and FA$^+$/MA$^+$/Cs$^+$ are unchanged from pure FAPbI$_3$, when sufficiently above the phase transition temperature. This implies that the cation dynamics (for these cations) are insensitive to both direct and indirect cation−cation interactions, perhaps due to the picosecond timescale of the rotation, as well as to minor changes in lattice parameters on substitution. The invariance of the FA$^+$ dynamics across different compositions aligns with the unchanged favorable optoelectronic properties compared to pristine FAPbI$_3$.

In contrast, the cation dynamics are affected by the underlying symmetry of the inorganic lattice. The rotational rates of FA$^+$ are suppressed in the vicinity of the cubic/ tetragonal phase transition, and therefore, the increase in the phase transition temperature on Cs$^+$ substitution causes changes in the room temperature dynamics.[66] Furthermore, we find that the perpendicular rotation of MA$^+$ is faster at room temperature in cubic FA$^+$/MA$^+$ and MA$^+$/GUA$^+$ compositions, as compared to tetragonal MAPbI$_3$. Given that most device-relevant perovskite compositions possess this

faster perpendicular rotation of MA$^+$, we speculate that it might be linked with improved optoelectronic properties of the material.

■ CONCLUSIONS

We developed a protocol to experimentally determine the activation energies (E_a) and correlation times (τ_c) for rotation about each principal axis of the formamidinium ion (FA$^+$) separately, by measuring all the ^{2}H and ^{14}N T_1 relaxation constants as a function of temperature and applying a rotational diffusional model.

We then extended this method to study state-of-the-art multi-cation FA$^+$/Cs$^+$, FA$^+$/MA$^+$, FA$^+$/MA$^+$/Cs$^+$, and MA$^+$/ GUA$^+$ compositions. We find that in all cases, there is at least one component of rotation for all three cations on the picosecond timescale at room temperature. MA$^+$ also has a faster component (0.1 ps), and GUA$^+$ also has a slower component (∼10 ps).

Notably, the observed motion is sensitive to the symmetry of the inorganic lattice but not directly to the degree of substitution. In particular, the FA$^+$ dynamics were found to be unchanged in all samples, except for slower rotation at room temperature upon Cs$^+$ substitution due to the higher phase-transition temperature. However, the perpendicular rotation of MA$^+$ is approximately a factor of two faster at room temperature in cubic FA$_x$MA$_{1-x}$PbI$_3$, as compared to tetragonal MAPbI$_3$.

Surprisingly, we found that for mechanosynthesized FA$_x$MA$_{1-x}$PbI$_3$, the ^{2}H relaxation of MA$^+$ is dominated at high temperatures by physical diffusion to paramagnetic defects. This phenomenon could be used in future to study ion migration and the formation of paramagnetic defects. Importantly, high-purity solution-processed samples did not exhibit this effect.

Having demonstrated this relaxometry methodology for MA$^+$, FA$^+$, and GUA$^+$, we note that it can be readily extended to understand the dynamics of other relevant cations used in hybrid perovskites, such as dimethylammonium (DMA$^+$)[95−97] and methylenediammonium (MDA$^+$).[58,98] We further highlight that by understanding the FA$^+$ cation dynamics, we were recently able to mitigate the detrimental ^{1}H relaxation by deuteration and enable dynamic nuclear polarization experiments that show the structure of a surface coating on a single thin film.[99] Overall, the complete picture of the cation dynamics presented here will help reveal the underlying causes of the beneficial optoelectronic properties seen in some hybrid perovskite formulations and thereby aid the design of perovskite solar cells with higher efficiencies in the future.

■ ASSOCIATED CONTENT

Data Availability Statement

All data presented here (raw NMR and XRD data) can be accessed at the following DOI: 10.5281/zenodo.7317848 and is available under the CC-BY-4.0 (Creative Commons Attribution-ShareAlike 4.0 International) license.

ⓢ Supporting Information

The Supporting Information is available free of charge at https://pubs.acs.org/doi/10.1021/jacs.2c10149.

> Experimental details, fitting analysis, and supplementary figures and notes (PDF)

■ AUTHOR INFORMATION

Corresponding Author

Lyndon Emsley − *Institut des Sciences et Ingéniere Chimiques, Ecole Polytechnique Fédérale de Lausanne (EPFL), CH-1015 Lausanne, Switzerland;* ⊙ orcid.org/0000-0003-1360-2572; Email: lyndon.emsley@epfl.ch

Authors

Aditya Mishra − *Institut des Sciences et Ingéniere Chimiques, Ecole Polytechnique Fédérale de Lausanne (EPFL), CH-1015 Lausanne, Switzerland*

Michael A. Hope − *Institut des Sciences et Ingéniere Chimiques, Ecole Polytechnique Fédérale de Lausanne (EPFL), CH-1015 Lausanne, Switzerland;* ⊙ orcid.org/0000-0002-4742-9336

Michael Grätzel − *Institut des Sciences et Ingéniere Chimiques, Ecole Polytechnique Fédérale de Lausanne (EPFL), CH-1015 Lausanne, Switzerland;* ⊙ orcid.org/0000-0002-0068-0195

Complete contact information is available at:
https://pubs.acs.org/10.1021/jacs.2c10149

Author Contributions

The manuscript was written through contributions of all authors. All authors have given approval to the final version of the manuscript.

Notes

The authors declare no competing financial interest.

■ ACKNOWLEDGMENTS

■ REFERENCES

(1) Grätzel, M. The light and shade of perovskite solar cells. *Nat. Mater.* **2014**, *13*, 838−842.

(2) Manser, J. S.; Christians, J. A.; Kamat, P. V. Intriguing Optoelectronic Properties of Metal Halide Perovskites. *Chem. Rev.* **2016**, *116*, 12956−13008.

(3) Gao, P.; Grätzel, M.; Nazeeruddin, M. K. Organohalide lead perovskites for photovoltaic applications. *Energy Environ. Sci.* **2014**, *7*, 2448−2463.

(4) Jeong, J.; Kim, M.; Seo, J.; Lu, H.; Ahlawat, P.; Mishra, A.; Yang, Y.; Hope, M. A.; Eickemeyer, F. T.; Kim, M.; Yoon, Y. J.; Choi, I. W.; Darwich, B. P.; Choi, S. J.; Jo, Y.; Lee, J. H.; Walker, B.; Zakeeruddin, S. M.; Emsley, L.; Rothlisberger, U.; Hagfeldt, A.; Kim, D. S.; Grätzel, M.; Kim, J. Y. Pseudo-halide anion engineering for α-FAPbI₃ perovskite solar cells. *Nature* **2021**, *592*, 381−385.

(5) Yoo, J. J.; Seo, G.; Chua, M. R.; Park, T. G.; Lu, Y. L.; Rotermund, F.; Kim, Y. K.; Moon, C. S.; Jeon, N. J.; Correa-Baena, J. P.; Bulovic, V.; Shin, S. S.; Bawendi, M. G.; Seo, J. Efficient perovskite solar cells via improved carrier management. *Nature* **2021**, *590*, 587.

(6) Best Research-Cell Efficiencies (NREL). https://www.nrel.gov/pv/assets/pdfs/best-research-cell-efficiencies-rev220630.pdf (accessed July 13, 2022).

(7) Snaith, H. J. Perovskites: The Emergence of a New Era for Low-Cost, High-Efficiency Solar Cells. *J. Phys. Chem. Lett.* **2013**, *4*, 3623−3630.

(8) Park, N. G. Perovskite solar cells: an emerging photovoltaic technology. *Mater. Today* **2015**, *18*, 65−72.

(9) Stoumpos, C. C.; Malliakas, C. D.; Kanatzidis, M. G. Semiconducting Tin and Lead Iodide Perovskites with Organic Cations: Phase Transitions, High Mobilities, and Near-Infrared Photoluminescent Properties. *Inorg. Chem.* **2013**, *52*, 9019−9038.

(10) Eperon, G. E.; Stranks, S. D.; Menelaou, C.; Johnston, M. B.; Herz, L. M.; Snaith, H. J. Formamidinium Lead Trihalide: A Broadly Tunable Perovskite for Efficient Planar Heterojunction Solar Cells. *Energy Environ. Sci.* **2014**, *7*, 982−988.

(11) Jodlowski, A. D.; Roldán-Carmona, C.; Grancini, G.; Salado, M.; Ralaiarisoa, M.; Ahmad, S.; Koch, N.; Camacho, L.; De Miguel, G.; Nazeeruddin, M. K. Large Guanidinium Cation Mixed with Methylammonium in Lead Iodide Perovskites for 19% Efficient Solar Cells. *Nat. Energy* **2017**, *2*, 972−979.

(12) Møller, C. K. Crystal Structure and Photoconductivity of Cæsium Plumbohalides. *Nature* **1958**, *182*, 1436.

(13) Eperon, G. E.; Paternò, G. M.; Sutton, R. J.; Zampetti, A.; Haghighirad, A. A.; Cacialli, F.; Snaith, H. J. Inorganic Caesium Lead Iodide Perovskite Solar Cells. *J. Mater. Chem. A* **2015**, *3*, 19688−19695.

(14) Lee, J.-W.; Tan, S.; Seok, S. I.; Yang, Y.; Park, N. G. Rethinking the A cation in halide perovskites. *Science* **2022**, *375*, No. eabj1186.

(15) Stoumpos, C. C.; Kanatzidis, M. G. The Renaissance of Halide Perovskites and Their Evolution as Emerging Semiconductors. *Acc. Chem. Res.* **2015**, *48*, 2791−2802.

(16) Choi, H.; Jeong, J.; Kim, H. B.; Kim, S.; Walker, B.; Kim, G. H.; Kim, J. Y. Cesium-doped methylammonium lead iodide perovskite light absorber for hybrid solar cells. *Nano Energy* **2014**, *7*, 80−85.

(17) Lee, J. W.; Kim, D. H.; Kim, H. S.; Seo, W.; Cho, S. M.; Park, N. G. Formamidinium and cesium hybridization for Photo- and Moisture-stable perovskite solar cell. *Adv. Energy Mater.* **2015**, *5*, 1501310.

(18) Yi, C.; Luo, J.; Meloni, S.; Boziki, A.; Ashari-Astani, N.; Grätzel, C.; Zakeeruddin, S. M.; Röthlisberger, U.; Grätzel, M. Entropic stabilization of mixed A-cation ABX₃ metal halide perovskites for high performance perovskite solar cells. *Energy Environ. Sci.* **2016**, *9*, 656−662.

(19) Li, Z.; Yang, M.; Park, J. S.; Wei, S. H.; Berry, J. J.; Zhu, K. Stabilizing Perovskite Structures by Tuning Tolerance Factor: Formation of Formamidinium and Cesium Lead Iodide Solid-State Alloys. *Chem. Mater.* **2016**, *28*, 284−292.

(20) Pellet, N.; Gao, P.; Gregori, G.; Yang, T. Y.; Nazeeruddin, M. K.; Maier, J.; Grätzel, M. Mixed-organic-cation perovskite photo-voltaics for enhanced solar-light harvesting. *Angew. Chem.* **2014**, *53*, 3151−3157.

(21) Lu, H.; Liu, Y.; Ahlawat, P.; Mishra, A.; Tress, W. R.; Eickemeyer, F. T.; Yang, Y.; Fu, F.; Wang, Z.; Avalos, C. E.; Carlsen, B. I.; Agarwalla, A.; Zhang, X.; Li, X.; Zhan, Y.; Zakeeruddin, S. M.; Emsley, L.; Rothlisberger, U.; Zheng, L.; Hagfeldt, A.; Grätzel, M. Vapor-assisted deposition of highly efficient, stable black-phase FAPbI₃ perovskite solar cells. *Science* **2020**, *370*, No. eabb8985.

(22) Saliba, M.; Matsui, T.; Seo, J.-Y.; Domanski, K.; Correa-Baena, J.-P.; Nazeeruddin, M. K.; Zakeeruddin, S. M.; Tress, W.; Abate, A.; Hagfeldt, A.; Grätzel, M. Cesium-containing triple cation perovskite solar cells: improved stability, reproducibility and high efficiency. *Energy Environ. Sci.* **2016**, *9*, 1989−1997.

(23) Jung, E. H.; Jeon, N. J.; Park, E. Y.; Moon, C. S.; Shin, T. J.; Yang, T. Y.; Noh, J. H.; Seo, J. Efficient, stable and scalable perovskite solar cells using poly(3-hexylthiophene). *Nature* **2019**, *567*, 511.

(24) Jeon, N. J.; Noh, J. H.; Yang, W. S.; Kim, Y. C.; Ryu, S.; Seo, J.; Seok, S. I. Compositional engineering of perovskite materials for high-performance solar cells. *Nature* **2015**, *517*, 476.

(25) Su, T. S.; Eickemeyer, F. T.; Hope, M. A.; Jahanbakhshi, F.; Mladenović, M.; Li, J.; Zhou, Z. W.; Mishra, A.; Yum, J. H.; Ren, D.; Krishna, A.; Ouellette, O.; Wei, T. C.; Zhou, H.; Huang, H. H.; Mensi, M. D.; Sivula, K.; Zakeeruddin, S. M.; Milić, J. V.; Hagfeldt, A.; Rothlisberger, U.; Emsley, L.; Zhang, H.; Grätzel, M. Crown Ether

Modulation Enables over 23% Efficient Formamidinium-Based Perovskite Solar Cells. *J. Am. Chem. Soc.* **2020**, *142*, 19980–19991.

(26) Wang, S. R.; Wang, A. L.; Hao, F. Toward stable lead halide perovskite solar cells: A knob on the A/X sites components. *iScience* **2022**, *25*, 103599.

(27) Anusca, I.; Balciunas, S.; Gemeiner, P.; Svirskas, S.; Sanlialp, M.; Lackner, G.; Fettkenhauer, C.; Belovickis, J.; Samulionis, V.; Ivanov, M.; Dkhil, B.; Banys, J.; Shvartsman, V. V.; Lupascu, D. C. Dielectric Response: Answer to Many Questions in the Methyl-ammonium Lead Halide Solar Cell Absorbers. *Adv. Energy Mater.* **2017**, *7*, 1700600.

(28) Juarez-Perez, E. J.; Sanchez, R. S.; Badia, L.; Garcia-Belmonte, G.; Kang, Y. S.; Mora-Sero, I.; Bisquert, J. Photoinduced Giant Dielectric Constant in Lead Halide Perovskite Solar Cells. *J. Phys. Chem. Lett.* **2014**, *5*, 2390–2394.

(29) La-o-vorakiat, C.; Xia, H. X.; Kadro, J.; Salim, T.; Zhao, D. M.; Ahmed, T.; Lam, Y. M.; Zhu, J. X.; Marcus, R. A.; Michel-Beyerle, M. E.; Chia, E. E. M. Phonon Mode Transformation Across the Orthorhombic-Tetragonal Phase Transition in a Lead Iodide Perov-skite CH$_3$NH$_3$PbI$_3$: A Terahertz Time-Domain Spectroscopy Approach. *J. Phys. Chem. Lett.* **2016**, *7*, 1–6.

(30) Wright, A. D.; Verdi, C.; Milot, R. L.; Eperon, G. E.; Pérez-Osorio, M. A.; Snaith, H. J.; Giustino, F.; Johnston, M. B.; Herz, L. M. Electron-phonon coupling in hybrid lead halide perovskites. *Nat. Commun.* **2016**, *7*, 11755.

(31) Wasylishen, R.; Knop, O.; Macdonald, J. Cation Rotation in Methylammonium Lead Halides. *Solid State Commun.* **1985**, *56*, 581.

(32) Fabini, D. H.; Siaw, T. A.; Stoumpos, C. C.; Laurita, G.; Olds, D.; Page, K.; Hu, J. G.; Kanatzidis, M. G.; Han, S.; Seshadri, R. Universal Dynamics of Molecular Reorientation in Hybrid Lead Iodide Perovskites. *J. Am. Chem. Soc.* **2017**, *139*, 16875–16884.

(33) Mozur, E. M.; Neilson, J. R. Cation Dynamics in Hybrid Halide Perovskites. *Annu. Rev. Mater. Res.* **2021**, *51*, 269–291.

(34) Liu, S.; Guo, R.; Xie, F. The effects of organic cation rotation in hybrid Organic-Inorganic Perovskites: A critical review. *Mater. Des.* **2022**, *221*, 110951.

(35) Lee, J. W.; Seo, S.; Nandi, P.; Jung, H. S.; Park, N. G.; Shin, H. Dynamic structural property of organic-inorganic metal halide perovskite. *iScience* **2021**, *24*, 101959.

(36) Herz, L. M. How Lattice Dynamics Moderate the Electronic Properties of Metal-Halide Perovskites. *J. Phys. Chem. Lett.* **2018**, *9*, 6853–6863.

(37) Crothers, T. W.; Milot, R. L.; Patel, J. B.; Parrott, E. S.; Schlipf, J.; Müller-Buschbaum, P.; Johnston, M. B.; Herz, L. M. Photon Reabsorption Masks Intrinsic Bimolecular Charge-Carrier Recombi-nation in CH$_3$NH$_3$PbI$_3$ Perovskite. *Nano Lett.* **2017**, *17*, 5782–5789.

(38) Sendner, M.; Nayak, P. K.; Egger, D. A.; Beck, S.; Müller, C.; Epding, B.; Kowalsky, W.; Kronik, L.; Snaith, H. J.; Pucci, A.; Lovrinčić, R. Optical phonons in methylammonium lead halide perovskites and implications for charge transport. *Mater. Horiz.* **2016**, *3*, 613–620.

(39) Chen, T. R.; Chen, W. L.; Foley, B. J.; Lee, J.; Ruff, J. P. C.; Ko, J. Y. P.; Brown, C. M.; Harriger, L. W.; Zhang, D. P.; Park, C. W.; Yoon, M.; Chang, Y. M.; Choi, J. J.; Lee, S. H. Origin of long lifetime of band-edge charge carriers in organic-inorganic lead iodide perovskites. *Proc. Natl. Acad. Sci. U.S.A.* **2017**, *114*, 7519–7524.

(40) Ambrosio, F.; Meggiolaro, D.; Mosconi, E.; De Angelis, F. Charge Localization, Stabilization, and Hopping in Lead Halide Perovskites: Competition between Polaron Stabilization and Cation Disorder. *ACS Energy Lett.* **2019**, *4*, 2013–2020.

(41) Gélvez-Rueda, M. C.; Cao, D. H.; Patwardhan, S.; Renaud, N.; Stoumpos, C. C.; Schatz, G. C.; Hupp, J. T.; Farha, O. K.; Savenije, T. J.; Kanatzidis, M. G.; Grozema, F. C. Effect of Cation Rotation on Charge Dynamics in Hybrid Lead Halide Perovskites. *J. Phys. Chem. C* **2016**, *120*, 16577–16585.

(42) Frost, J. M.; Butler, K. T.; Brivio, F.; Hendon, C. H.; van Schilfgaarde, M.; Walsh, A. Atomistic Origins of High-Performance in Hybrid Halide Perovskite Solar Cells. *Nano Lett.* **2014**, *14*, 2584–2590.

(43) Zhu, X. Y.; Podzorov, V. Charge Carriers in Hybrid Organic-Inorganic Lead Halide Perovskites Might Be Protected as Large Polarons. *J. Phys. Chem. Lett.* **2015**, *6*, 4758–4761.

(44) Kim, M.; Im, J.; Freeman, A. J.; Ihm, J.; Jin, H. Switchable S = 1/2 and J = 1/2 Rashba bands in ferroelectric halide perovskites. *Proc. Natl. Acad. Sci. U.S.A.* **2014**, *111*, 6900–6904.

(45) Leguy, A. M.; Frost, J. M.; McMahon, A. P.; Sakai, V. G.; Kockelmann, W.; Law, C.; Li, X.; Foglia, F.; Walsh, A.; O'Regan, B. C.; Nelson, J.; Cabral, J. T.; Barnes, P. R. F. The dynamics of methylammonium ions in hybrid organic-inorganic perovskite solar cells. *Nat. Commun.* **2015**, *6*, 7124.

(46) Swainson, I. P.; Stock, C.; Parker, S. F.; Van Eijck, L.; Russina, M.; Taylor, J. W. From soft harmonic phonons to fast relaxational dynamics in CH$_3$NH$_3$PbBr$_3$. *Phys. Rev. B: Condens. Matter Mater. Phys.* **2015**, *92*, 100303.

(47) Chen, T.; Foley, B. J.; Ipek, B.; Tyagi, M.; Copley, J. R. D.; Brown, C. M.; Choi, J. J.; Lee, S. H. Rotational dynamics of organic cations in the CH$_3$NH$_3$PbI$_3$ perovskite. *Phys. Chem. Chem. Phys.* **2015**, *17*, 31278–31286.

(48) Druzbicki, K.; Pinna, R. S.; Rudic, S.; Jura, M.; Gorini, G.; Fernandez-Alonso, F. Unexpected Cation Dynamics in the Low-Temperature Phase of Methylammonium Lead Iodide: The Need for Improved Models. *J. Phys. Chem. Lett.* **2016**, *7*, 4701–4709.

(49) Li, B.; Kawakita, Y.; Liu, Y. C.; Wang, M. C.; Matsuura, M.; Shibata, K.; Ohira-Kawamura, S.; Yamada, T.; Lin, S. C.; Nakajima, K. J.; Liu, S. Z. Polar rotor scattering as atomic-level origin of low mobility and thermal conductivity of perovskite CH$_3$NH$_3$PbI$_3$. *Nat. Commun.* **2017**, *8*, 16086.

(50) Poglitsch, A.; Weber, D. Dynamic disorder in methylammo-niumtrihalogenoplumbates (II) observed by millimeter-wave spec-troscopy. *J. Chem. Phys.* **1987**, *87*, 6373–6378.

(51) Bakulin, A. A.; Selig, O.; Bakker, H. J.; Rezus, Y. L. A.; Müller, C.; Glaser, T.; Lovrincic, R.; Sun, Z. H.; Chen, Z. Y.; Walsh, A.; Frost, J. M.; Jansen, T. L. C. Real-Time Observation of Organic Cation Reorientation in Methylammonium Lead Iodide Perovskites. *J. Phys. Chem. Lett.* **2015**, *6*, 3663–3669.

(52) Selig, O.; Sadhanala, A.; Müller, C.; Lovrincic, R.; Chen, Z.; Rezus, Y. L. A.; Frost, J. M.; Jansen, T. L. C.; Bakulin, A. A. Organic Cation Rotation and Immobilization in Pure and Mixed Methyl-ammonium Lead-Halide Perovskites. *J. Am. Chem. Soc.* **2017**, *139*, 4068–4074.

(53) Kubicki, D. J.; Prochowicz, D.; Hofstetter, A.; Péchy, P.; Zakeeruddin, S. M.; Grätzel, M.; Emsley, L. Cation Dynamics in Mixed-Cation (MA)$_x$(FA)$_{1-x}$PbI$_3$ Hybrid Perovskites from Solid-State NMR. *J. Am. Chem. Soc.* **2017**, *139*, 10055–10061.

(54) Bernard, G. M.; Wasylishen, R. E.; Ratcliffe, C. I.; Terskikh, V.; Wu, Q.; Buriak, J. M.; Hauger, T. Methylammonium Cation Dynamics in Methylammonium Lead Halide Perovskites: A Solid-State NMR Perspective. *J. Phys. Chem. A* **2018**, *122*, 1560–1573.

(55) Xu, Q.; Eguchi, T.; Nakayama, H.; Nakamura, N.; Kishita, M. Molecular Motions and Phase-Transitions in Solid CH$_3$NH$_3$PbCl$_3$, CH$_3$NH$_3$PbBr$_3$, CH$_3$NH$_3$PbI$_3$, as Studied by NMR and NQR. *Z. Naturforsch., A: Phys. Sci.* **1991**, *46*, 240–246.

(56) Kubicki, D. J.; Stranks, S. D.; Grey, C. P.; Emsley, L. NMR spectroscopy probes microstructure, dynamics and doping of metal halide perovskites. *Nat. Rev. Chem.* **2021**, *5*, 624–645.

(57) Senocrate, A.; Moudrakovski, I.; Maier, J. Short-range ion dynamics in methylammonium lead iodide by multinuclear solid state NMR and ^{127}I NQR. *Phys. Chem. Chem. Phys.* **2018**, *20*, 20043–20055.

(58) Kim, G.; Min, H.; Lee, K. S.; Lee, D. Y.; Yoon, S. M.; Seok, S. I. Impact of strain relaxation on performance of α-formamidinium lead iodide perovskite solar cells. *Science* **2020**, *370*, 108.

(59) Taylor, V. C. A.; Tiwari, D.; Duchi, M.; Donaldson, P. M.; Clark, I. P.; Fermin, D. J.; Oliver, T. A. A. Investigating the Role of the Organic Cation in Formamidinium Lead Iodide Perovskite Using Ultrafast Spectroscopy. *J. Phys. Chem. Lett.* **2018**, *9*, 895–901.

(60) Drużbicki, K.; Laven, R.; Armstrong, J.; Malavasi, L.; Fernandez-Alonso, F.; Karlsson, M. Cation Dynamics and Structural

Stabilization in Formamidinium Lead Iodide Perovskites. *J. Phys. Chem. Lett.* **2021**, *12*, 3503−3508.

(61) Mozur, E. M.; Hope, M. A.; Trowbridge, J. C.; Halat, D. M.; Daemen, L. L.; Maughan, A. E.; Prisk, T. R.; Grey, C. P.; Neilson, J. R. Cesium Substitution Disrupts Concerted Cation Dynamics in Formamidinium Hybrid Perovskites. *Chem. Mater.* **2020**, *32*, 6266−6277.

(62) Reif, B.; Ashbrook, S. E.; Emsley, L.; Hong, M. Solid-state NMR spectroscopy. *Nat. Rev. Methods Primers* **2021**, *1*, 2.

(63) Schmidt-Rohr, K.; Spiess, H. W.*Multidimensional Solid-State NMR and Polymers*; Elsevier, 2012.

(64) Min, G.; Yun, Y.; Choi, H. J.; Lee, S.; Joo, J. Hydrogen halide-free synthesis of organohalides for organometal trihalide perovskite solar cells. *J. Ind. Eng. Chem.* **2020**, *89*, 375−382.

(65) d'Espinose de LaCaillerie, J.-B.; Fretigny, C.; Massiot, D. MAS NMR spectra of quadrupolar nuclei in disordered solids: The Czjzek model. *J. Magn. Reson.* **2008**, *192*, 244−251.

(66) Kawachi, S.; Atsumi, M.; Saito, N.; Ohashi, N.; Murakami, Y.; Yamaura, J.-i. Structural and Thermal Properties in Formamidinium and Cs-Mixed Lead Halides. *J. Phys. Chem. Lett.* **2019**, *10*, 6967−6972.

(67) Fabini, D. H.; Stoumpos, C. C.; Laurita, G.; Kaltzoglou, A.; Kontos, A. G.; Falaras, P.; Kanatzidis, M. G.; Seshadri, R. Reentrant Structural and Optical Properties and Large Positive Thermal Expansion in Perovskite Formamidinium Lead Iodide. *Angew. Chem.* **2016**, *55*, 15392−15396.

(68) Huntress, W. T., Jr.The study of anisotropic rotation of molecules in liquids by NMR quadrupolar relaxation. *Advances in Magnetic and Optical Resonance*; Elsevier, 1970; Vol. *4*, pp 1−37. DOI: 10.1016/b978-0-12-025504-7.50007-6

(69) Chen, T.; Foley, B. J.; Park, C.; Brown, C. M.; Harriger, L. W.; Lee, J.; Ruff, J.; Yoon, M.; Choi, J. J.; Lee, S. H. Entropy-driven structural transition and kinetic trapping in formamidinium lead iodide perovskite. *Sci. Adv.* **2016**, *2*, No. e1601650.

(70) Nandi, P.; Li, Z.; Kim, Y.; Ahn, T. K.; Park, N. G.; Shin, H. Stabilizing Mixed Halide Lead Perovskites against Photoinduced Phase Segregation by A-Site Cation Alloying. *ACS Energy Lett.* **2021**, *6*, 837−847.

(71) Knight, A. J.; Borchert, J.; Oliver, R. D. J.; Patel, J. B.; Radaelli, P. G.; Snaith, H. J.; Johnston, M. B.; Herz, L. M. Halide Segregation in Mixed-Halide Perovskites: Influence of A-Site Cations. *ACS Energy Lett.* **2021**, *6*, 799−808.

(72) Xu, J. X.; Boyd, C. C.; Yu, Z. S. J.; Palmstrom, A. F.; Witter, D. J.; Larson, B. W.; France, R. M.; Werner, J.; Harvey, S. P.; Wolf, E. J.; Weigand, W.; Manzoor, S.; van Hest, M. F. A. M.; Berry, J. J.; Luther, J. M.; Holman, Z. C.; McGehee, M. D. Triple-halide wide-band gap perovskites with suppressed phase segregation for efficient tandems. *Science* **2020**, *367*, 1097.

(73) Li, N. X.; Tao, S. X.; Chen, Y. H.; Niu, X. X.; Onwudinanti, C. K.; Hu, C.; Qiu, Z. W.; Xu, Z. Q.; Zheng, G. H. J.; Wang, L. G.; Zhang, Y.; Li, L.; Liu, H. F.; Lun, Y. Z.; Hong, J. W.; Wang, X. Y.; Liu, Y. Q.; Xie, H. P.; Gao, Y. L.; Bai, Y.; Yang, S. H.; Brocks, G.; Chen, Q.; Zhou, H. P. Cation and anion immobilization through chemical bonding enhancement with fluorides for stable halide perovskite solar cells. *Nat. Energy* **2019**, *4*, 408−415.

(74) Li, F. Z.; Deng, X.; Qi, F.; Li, Z.; Liu, D. J.; Shen, D.; Qin, M. C.; Wu, S. F.; Lin, F.; Jang, S. H.; Zhang, J.; Lu, X. H.; Lei, D. Y.; Lee, C. S.; Zhu, Z. L.; Jen, A. K. Y. Regulating Surface Termination for Efficient Inverted Perovskite Solar Cells with Greater Than 23% Efficiency. *J. Am. Chem. Soc.* **2020**, *142*, 20134−20142.

(75) Kubicki, D. J.; Prochowicz, D.; Hofstetter, A.; Zakeeruddin, S. M.; Grätzel, M.; Emsley, L. Phase Segregation in Cs-, Rb- and K-Doped Mixed-Cation $(MA)_x(FA)_{1-x}PbI_3$ Hybrid Perovskites from Solid-State NMR. *J. Am. Chem. Soc.* **2017**, *139*, 14173−14180.

(76) Francisco-López, A.; Charles, B.; Alonso, M. I.; Garriga, M.; Campoy-Quiles, M.; Weller, M. T.; Goñi, A. R. Phase Diagram of Methylammonium/Formamidinium Lead Iodide Perovskite Solid Solutions from Temperature-Dependent Photoluminescence and Raman Spectroscopies. *J. Phys. Chem. C* **2020**, *124*, 3448−3458.

(77) McClung, R. E. D.Spin−Rotation Relaxation Theory. *eMagRes*; John Wiley & Sons, Ltd, 2007.

(78) Józef, K.; Lena, M.*Nuclear Spin Relaxation in Liquids: Theory, Experiments, and Applications*; CRC Press, 2017.

(79) Pell, A. J.; Pintacuda, G.; Grey, C. P. Paramagnetic NMR in solution and the solid state. *Prog. Nucl. Magn. Reson. Spectrosc.* **2019**, *111*, 1−271.

(80) Hayashi, S. Effects of magic-angle spinning on spin-lattice relaxations in talc. *Solid State Nucl. Magn. Reson.* **1994**, *3*, 323−330.

(81) De Marco, N.; Zhou, H. P.; Chen, Q.; Sun, P. Y.; Liu, Z. H.; Meng, L.; Yao, E. P.; Liu, Y. S.; Schiffer, A.; Yang, Y. Guanidinium: A Route to Enhanced Carrier Lifetime and Open-Circuit Voltage in Hybrid Perovskite Solar Cells. *Nano Lett.* **2016**, *16*, 1009−1016.

(82) Gao, L. L.; Li, X. T.; Liu, Y.; Fang, J. J.; Huang, S.; Spanopoulos, I.; Li, X. L.; Wang, Y.; Chen, L.; Yang, G. J.; Kanatzidis, M. G. Incorporated Guanidinium Expands the $CH_3NH_3PbI_3$ Lattice and Enhances Photovoltaic Performance. *ACS Appl. Mater. Interfaces* **2020**, *12*, 43885−43891.

(83) Prochowicz, D.; Tavakoli, M. M.; Alanazi, A. Q.; Trivedi, S.; Tavakoli Dastjerdi, H. T.; Zakeeruddin, S. M.; Grätzel, M.; Yadav, P. Charge Accumulation, Recombination, and Their Associated Time Scale in Efficient $(GUA)_x(MA)_{1-x}PbI_3$-Based Perovskite Solar Cells. *ACS Omega* **2019**, *4*, 16840−16846.

(84) Giorgi, G.; Fujisawa, J. I.; Segawa, H.; Yamashita, K. Organic-Inorganic Hybrid Lead Iodide Perovskite Featuring Zero Dipole Moment Guanidinium Cations: A Theoretical Analysis. *J. Phys. Chem. C* **2015**, *119*, 4694−4701.

(85) Nimerovsky, E.; Gupta, R.; Yehl, J.; Li, M. Y.; Polenova, T.; Goldbourt, A. Phase-modulated LA-REDOR: A robust, accurate and efficient solid-state NMR technique for distance measurements between a spin-1/2 and a quadrupole spin. *J. Magn. Reson.* **2014**, *244*, 107−113.

(86) Oja, T. Nitrogen-14 nuclear quadrupole resonance study of the guanidinium ion. *J. Chem. Phys.* **1973**, *59*, 2668−2675.

(87) Ratcliffe, C. I. Nuclear magnetic resonance studies of molecular motion in guanidinium chloride, bromide, and iodide. *Can. J. Chem.* **1985**, *63*, 1239−1244.

(88) Kieslich, G.; Sun, S. J.; Cheetham, A. K. Solid-state principles applied to organic-inorganic perovskites: new tricks for an old dog. *Chem. Sci.* **2014**, *5*, 4712−4715.

(89) Hoefler, S. F.; Trimmel, G.; Rath, T. Progress on lead-free metal halide perovskites for photovoltaic applications: a review. *Monatsh. Chem.* **2017**, *148*, 795−826.

(90) Bloembergen, N.; Purcell, E. M.; Pound, R. V. Relaxation Effects in Nuclear Magnetic Resonance Absorption. *Phys. Rev.* **1948**, *73*, 679−712.

(91) Even, J.; Carignano, M.; Katan, C. Molecular disorder and translation/rotation coupling in the plastic crystal phase of hybrid perovskites. *Nanoscale* **2016**, *8*, 6222−6236.

(92) Vold, R. L.; Hoatson, G. L. Effects of jump dynamics on solid state nuclear magnetic resonance line shapes and spin relaxation times. *J. Magn. Reson.* **2009**, *198*, 57−72.

(93) Whitfield, P. S.; Herron, N.; Guise, W. E.; Page, K.; Cheng, Y. Q.; Milas, I.; Crawford, M. K. Structures, Phase Transitions and Tricritical Behavior of the Hybrid Perovskite Methyl Ammonium Lead Iodide. *Sci. Rep.* **2016**, *6*, 35685.

(94) Franz, A.; Többens, D. M.; Lehmann, F.; Kärgell, M.; Schorr, S. The influence of deuteration on the crystal structure of hybrid halide perovskites: a temperature-dependent neutron diffraction study of $FAPbBr_3$. *Acta Crystallogr., Sect. B: Struct. Sci.* **2020**, *76*, 267−274.

(95) Franssen, W. M. J.; Bruijnaers, B. J.; Portengen, V. H. L.; Kentgens, A. P. M. Dimethylammonium Incorporation in Lead Acetate Based MAPbI3 Perovskite Solar Cells. *Chemphyschem* **2018**, *19*, 3107−3115.

(96) Ray, A.; Martín-García, B.; Moliterni, A.; Casati, N.; Boopathi, K. M.; Spirito, D.; Goldoni, L.; Prato, M.; Giacobbe, C.; Giannini, C.; Di Stasio, F.; Krahne, R.; Manna, L.; Abdelhady, A. L. Mixed Dimethylammonium/Methylammonium Lead Halide Perovskite

Crystals for Improved Structural Stability and Enhanced Photo-detection. *Adv. Mater.* **2022**, *34*, 2106160.

(97) Mishra, A.; Kubicki, D. J.; Boziki, A.; Chavan, R. D.; Dankl, M.; Mladenović, M.; Prochowicz, D.; Grey, C. P.; Rothlisberger, U.; Emsley, L. Interplay of Kinetic and Thermodynamic Reaction Control Explains Incorporation of Dimethylammonium Iodide into $CsPbI_3$. *ACS Energy Lett.* **2022**, *7*, 2745−2752.

(98) Min, H.; Kim, M.; Lee, S. U.; Kim, H.; Kim, G.; Choi, K.; Lee, J. H.; Seok, S. I. Efficient, stable solar cells by using inherent bandgap of α-phase formamidinium lead iodide. *Science* **2019**, *366*, 749.

(99) Mishra, A.; Hope, M. A.; Almalki, M.; Pfeifer, L.; Zakeeruddin, S. M.; Grätzel, M.; Emsley, L. Dynamic Nuclear Polarization Enables NMR of Surface Passivating Agents on Hybrid Perovskite Thin Films. *J. Am. Chem. Soc.* **2022**, *144*, 15175−15184.